



LQR-Based Adaptive Virtual Synchronous Machine for Power Systems With High Inverter Penetration

Uros Markovic , *Student Member, IEEE*, Zhongda Chu, *Student Member, IEEE*,
Petros Aristidou , *Member, IEEE*, and Gabriela Hug, *Senior Member, IEEE*

Abstract—This paper presents a novel virtual synchronous machine controller for converters in power systems with a high share of renewable resources. Using a linear quadratic regulator-based optimization technique, the optimal state feedback gain is determined to adaptively adjust the emulated inertia and damping constants according to the frequency disturbance in the system, while simultaneously preserving a tradeoff between the critical frequency limits and the required control effort. Two control designs are presented and compared against the open-loop model. The proposed controllers are integrated into a state-of-the-art converter control scheme and verified through electromagnetic transient (EMT) simulations.

Index Terms—Linear-quadratic regulator (LQR), virtual synchronous machine (VSM), voltage source converter (VSC), swing equation, adaptive control.

I. INTRODUCTION

THE current trends towards green energy have led to all-time-high penetration levels of renewable energy sources. Unlike traditional Synchronous Machines (SMs), these distributed units are usually connected to the grid through fast-acting power inverters which electrically decouple the kinetic energy stored in the rotating masses of the generator from the network, thus resulting in low-inertia systems [1]. The loss of rotational inertia can have devastating effects on system dynamics, with large frequency deviations potentially triggering undesirable events such as load-shedding and large-scale blackouts, as indicated in [2]. However, this study also shows that grid-scale energy storage devices can be employed for providing fast frequency support in isolated systems with high shares of renewables; such support can be incorporated within a control scheme of a grid-forming Voltage Source Converter (VSC) [3].

One of the most common VSC control approaches in the literature is a Virtual Synchronous Machine (VSM), an emulation

technique based on some form of a swing equation equivalent that “slows down” the transient system dynamics [4]. While the sole design and implementation can vary from a detailed 7th order SM model to a representation of only the swing equation [5], it is often based on the assumption that the generator can produce or absorb an infinite amount of power over short periods of time. Hence, the dynamical limitations of a DC-side capacitor are neglected, which proves to be an issue for real-world applications [6]. This problem was addressed in [7] with a distributed virtual inertia approach that regulates the DC-link voltages such that the capacitors are aggregated into a large unit for frequency support. However, it is implemented via a basic proportional frequency controller and does not take into account the overall control effort, i.e., the value of the stored energy used for regulation. Additionally, a derivative control term corresponding to the control of Rate-of-Change-of-Frequency (RoCoF) can be integrated for containing fast and excessive frequency excursions, either as a contribution to the traditional droop-like primary frequency control [8], or component of a more complex heuristic [9] or optimization-based [10] online-tuning of a VSM. Motivated by the same approach, a subgroup of so-called *interval-based* controllers emerged [11], [12], where a sign of the trigger signal $\varrho = (\Delta\omega)(d\omega/dt)$ is used to indicate whether the unit is in the “accelerating” or “decelerating” mode. The nature of the mode would then heuristically determine the level of virtual inertia and/or damping in a gain-scheduling fashion. Nonetheless, all concepts mentioned above focus solely on the overall frequency improvement, while disregarding the costs and energy resources required for such regulation.

We have previously addressed this problem in [13], with an LQR-based adaptive virtual inertia controller that *optimally* adjusts the respective inertia gain to achieve a trade-off between the two objectives. However, it was implemented on a simplified, single-inverter test case, and the adaptive damping was not taken into account. This paper extends the work in [13] in several directions by (i) deriving a uniform multi-machine frequency model; (ii) including adaptive damping and proposing two novel control methods; (iii) providing a formulation for a decentralized multi-inverter control scheme; and (iv) incorporating the controllers into a detailed VSC model and verifying it through electromagnetic transient (EMT) simulations. To the best knowledge of the authors, such uniform approach has not been proposed in the literature thus far.

The remainder of the paper is structured as follows. In Section II, the multi-machine system dynamics are

Manuscript received July 9, 2018; revised October 23, 2018; accepted November 18, 2018. Date of publication December 17, 2018; date of current version June 20, 2019. This work was supported by the *European Union's Horizon 2020 research and innovation programme* under Grant 691800. This paper reflects only the authors' views and the European Commission is not responsible for any use that may be made of the information it contains. Paper no. TSTE-00677-2018 (Uros Markovic and Zhongda Chu contributed equally to this work.) (Corresponding author: Uros Markovic.)

U. Markovic, Z. Chu, and G. Hug are with the Power Systems Laboratory, ETH Zurich, Zurich 8092, Switzerland (e-mail: markovic@eeh.ee.ethz.ch; zhchu@student.ethz.ch; hug@eeh.ee.ethz.ch).

P. Aristidou is with the School of Electronic and Electrical Engineering, University of Leeds, Leeds LS2 9JT, U.K. (e-mail: p.aristidou@leeds.ac.uk).

Color versions of one or more of the figures in this paper are available online at <http://ieeexplore.ieee.org>.

Digital Object Identifier 10.1109/TSTE.2018.2887147

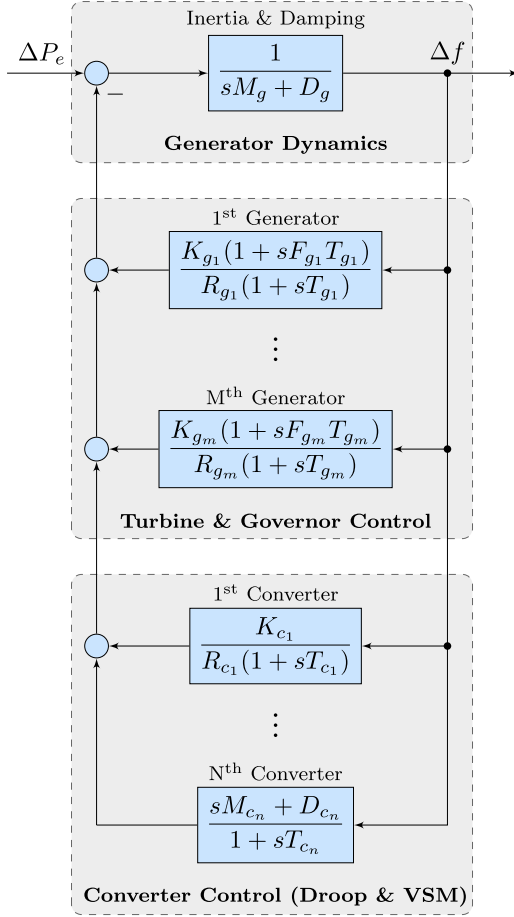


Fig. 1. Uniform system frequency dynamics model.

investigated, and the respective frequency metrics are analytically derived. Section III describes the adaptive VSM formulation and proposes two novel control designs, which are subsequently implemented within a detailed VSC control scheme presented in Section IV. Section V showcases the EMT simulation results and compares the methods, whereas Section VI draws the main conclusions and discusses the outlook of the study.

II. SYSTEM FREQUENCY DYNAMICS

A. Primary Frequency Control in Low Inertia Systems

The first goal is to derive a simplified, but sufficiently accurate, uniform frequency response model of a low-inertia system. Let us observe such system consisting of multiple *traditional* (subscript g) and *converter-based* (subscript c) generators, as depicted in Fig. 1. The generator dynamics are described by the swing equation, with M_g and D_g denoting the normalized inertia and damping constants of the generators:

$$M_g = \frac{\sum_{i \in \mathcal{N}_g} M_{g_i} P_{g_i}}{P_{b_g}}, \quad D_g = \frac{\sum_{i \in \mathcal{N}_g} D_{g_i} P_{g_i}}{P_{b_g}} \quad (1)$$

where $i \in \mathcal{N}_g$ is the set of traditional synchronous generators and P_{g_i} are their nominal powers; P_{b_g} refers to the base power

of the generators, i.e., a sum of nominal powers of all connected generation units. The low-order model proposed in [14] is used for modelling the governor droop and turbine dynamics; T_{g_i} are the turbine time constants, R_{g_i} and K_{g_i} are the respective droop and mechanical power gain factor, while F_{g_i} denotes the fraction of total power generated by the turbines of synchronous machines. Furthermore, we incorporate the impact of grid-forming converters, as they are the only type of PE-interfaced units providing frequency support [3], [15]. A particular focus is set on droop and VSM-based control schemes, as two of the currently most prevalent emulation techniques in the literature [5], which in fact have equivalent properties in the forming mode of operation [16]. Hence, the set of grid-forming converters providing either droop (\mathcal{N}_d) or VSM (\mathcal{N}_v) control is represented by $\mathcal{N}_c = \mathcal{N}_d \cup \mathcal{N}_v$. In Fig. 1, T_{c_m} are the time constants of all converters $m \in \mathcal{N}_c$, R_{c_j} and K_{c_j} are the respective droop and mechanical power gain factors for $j \in \mathcal{N}_d$, whereas M_{c_k} and D_{c_k} denote the normalized virtual inertia and damping constants of converters $k \in \mathcal{N}_v$.

B. Analytic Formulation of Frequency Metrics

From Fig. 1 we can now derive a transfer function $G(s)$ of a general-order system dynamics, as follows:

$$G(s) = \frac{\Delta f}{\Delta P_e} = \left(\underbrace{(sM_g + D_g) + \sum_{i \in \mathcal{N}_g} \frac{K_{g_i}(1 + sF_{g_i}T_{g_i})}{R_{g_i}(1 + sT_{g_i})}}_{\text{traditional generators}} + \underbrace{\sum_{j \in \mathcal{N}_d} \frac{K_{c_j}}{R_{c_j}(1 + sT_{c_j})}}_{\text{droop converters}} + \underbrace{\sum_{k \in \mathcal{N}_v} \frac{sM_{c_k} + D_{c_k}}{1 + sT_{c_k}}}_{\text{VSM converters}} \right)^{-1} \quad (2)$$

Based on the sensitivity of the frequency response to governor parameters, it was previously shown in [17] that the frequency nadir of the SM-based system is the least sensitive to the governor time constant. Hence, assuming equal time constants ($T_{g_i} = T$) for all synchronous machines is a reasonable simplification. Additionally, the inverter time constants are approximately 2-3 orders of magnitude lower than the ones of synchronous machines, which justifies $T \gg T_{c_m} \approx 0$. Now we can transform (2) into the following expression:

$$G(s) = \frac{1}{MT} \frac{1 + sT}{s^2 + 2\zeta\omega_n s + \omega_n^2} \quad (3)$$

where the natural frequency (ω_n) and damping ratio (ζ) are computed as

$$\omega_n = \sqrt{\frac{D + R_g}{MT}}, \quad \zeta = \frac{M + T(D + F_g)}{2\sqrt{MT(D + R_g)}} \quad (4)$$

and the respective parameters are defined as follows:

$$M = \frac{M_g P_{b_g} + M_c P_{b_c}}{P_{b_g} + P_{b_c}} \quad (5a)$$

$$D = \frac{D_g P_{b_g} + D_c P_{b_c} + R_c P_{b_c}}{P_{b_g} + P_{b_c}} \quad (5b)$$

$$F_g = \sum_{i \in \mathcal{N}_g} \frac{K_{g_i} F_{g_i}}{R_{g_i}} \frac{P_{g_i}}{P_{b_g}} \quad (5c)$$

$$R_g = \sum_{i \in \mathcal{N}_g} \frac{K_{g_i}}{R_{g_i}} \frac{P_{g_i}}{P_{b_g}} \quad (5d)$$

$$R_c = \sum_{j \in \mathcal{N}_d} \frac{K_{c_j}}{R_{c_j}} \frac{P_{c_j}}{P_{b_c}} \quad (5e)$$

$$M_c = \sum_{k \in \mathcal{N}_v} M_{c_k} \frac{P_{c_k}}{P_{b_c}} \quad (5f)$$

$$D_c = \sum_{k \in \mathcal{N}_v} D_{c_k} \frac{P_{c_k}}{P_{b_c}} \quad (5g)$$

It should be noted that the P_{g_i}/P_{b_g} and P_{c_i}/P_{b_c} terms in (5c)-(5g) come from per unit normalization, with P_{b_c} being the base power of all converter units. The expressions in (5a) and (5b) indicate that the emulated inertia and damping through VSM, as well as the droop control gains, contribute proportionally to the overall inertia and damping of the system.

Assuming a stepwise disturbance in the electrical power $\Delta P_e(s) = -\Delta P/s$, the time-domain expression for frequency deviation ($\omega(t) \equiv \Delta f(t)$) can be derived as:

$$\begin{aligned} \omega(t) = & -\frac{\Delta P}{MT\omega_n^2} \\ & -\frac{\Delta P}{M\omega_d} e^{-\zeta\omega_n t} \left(\sin(\omega_d t) - \frac{1}{\omega_n T} \sin(\omega_d t + \phi) \right) \end{aligned} \quad (6)$$

with the introduction of new variables

$$\omega_d = \omega_n \sqrt{1 - \zeta^2}, \quad \phi = \sin^{-1} \left(\sqrt{1 - \zeta^2} \right) \quad (7)$$

The time instance of frequency nadir (t_m) can be determined by observing the RoCoF, i.e., finding the instance at which the derivative of the frequency is equal to zero:

$$\dot{\omega}(t_m) = 0 \implies t_m = \frac{1}{\omega_d} \tan^{-1} \left(\frac{\omega_d}{\zeta\omega_n - T^{-1}} \right) \quad (8)$$

Substituting t_m into (6) and conducting a set of mathematical transformations yields the value of frequency nadir as:

$$\omega_{\max} = -\frac{\Delta P}{D + R_g} \left(1 + \sqrt{\frac{T(R_g - F_g)}{M}} e^{-\zeta\omega_n t_m} \right) \quad (9)$$

The maximum RoCoF occurs at $t_r = 0^+$ and is equal to

$$\dot{\omega}_{\max} = \dot{\omega}(t_r) = -\frac{\Delta P}{M} \quad (10)$$

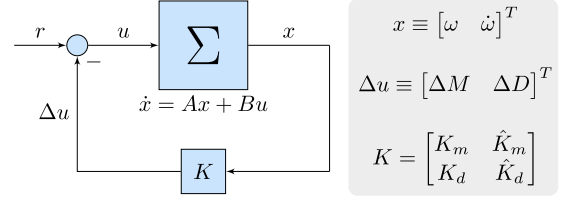


Fig. 2. State feedback control for adaptive VSM approach.

By analyzing expressions (9)-(10)¹ we can conclude that the two frequency metrics of interest (nadir and RoCoF) are directly dependent on total inertia and damping constants, both of which can be regulated through *adaptive* VSM control gains: RoCoF explicitly as $\dot{\omega}_{\max} \sim M^{-1}$, and nadir through a highly non-linear function $\omega_{\max} = f_{\omega}(M, D)$ given in (9).

III. ADAPTIVE VIRTUAL SYNCHRONOUS MACHINE

A. Non-Linear System Model

After the disturbance has been applied, i.e., $\forall t \in [0^+, +\infty)$ ΔP can be considered a constant, thus transforming (3) into the following expression:

$$\ddot{\omega} = -2\zeta\omega_n\dot{\omega} - \omega_n^2\omega + \frac{\Delta P}{MT} \quad (11)$$

Combining (4) and (11) yields a state-space representation of the form:

$$\begin{bmatrix} \dot{\omega} \\ \ddot{\omega} \end{bmatrix} = \begin{bmatrix} 0 & I \\ -\frac{D+R_g}{MT} & -(\frac{1}{T} + \frac{D+F_g}{M}) \end{bmatrix} \begin{bmatrix} \omega \\ \dot{\omega} \end{bmatrix} + \begin{bmatrix} 0 \\ \frac{\Delta P}{TM} \end{bmatrix} \quad (12)$$

with $x = [\omega \ \dot{\omega}]^T$ and $x_0 = [0 \ \dot{\omega}(0^+)]^T$ being the state vector and respective initial condition.

Let us now consider controlling the total inertia and damping of the system depicted in Fig. 2 by regulating the converters' VSM parameters through a state feedback control, i.e.,

$$\underbrace{\begin{bmatrix} M \\ D \end{bmatrix}}_u = \underbrace{\begin{bmatrix} M^* \\ D^* \end{bmatrix}}_{u^*} + \underbrace{\begin{bmatrix} \Delta M \\ \Delta D \end{bmatrix}}_{\Delta u} = \underbrace{\begin{bmatrix} M^* \\ D^* \end{bmatrix}}_x - \underbrace{\begin{bmatrix} K_m & \hat{K}_m \\ K_d & \hat{K}_d \end{bmatrix}}_K \underbrace{\begin{bmatrix} \omega \\ \dot{\omega} \end{bmatrix}}_x \quad (13)$$

where M^* and D^* are the total inertia and damping constants of the system before the disturbance; (K_m, \hat{K}_m) and (K_d, \hat{K}_d) represent the proportional feedback control gains for inertia and damping, respectively. It can be computed from (12)-(13) that such system would yield the following steady-state point:

$$\dot{x} = 0 \implies x_{ss} = [\omega_{ss}, \dot{\omega}_{ss}]^T = \left[\frac{\Delta P}{D^* + R_g} \ 0 \right]^T \quad (14)$$

The main goal of the work presented in this paper is to obtain the control gains K that would guarantee an *optimal* balance between the frequency regulation and the required energy use via adaptive control. Such balance can be achieved through the minimization of a quadratic objective function, with separate

¹The "max" term denotes the maximum absolute value of the deviation.

cost terms for frequency deviation (Q) and overall control effort (R), i.e.

$$\min_{x,u} \int_0^\infty (x^T Q x + u^T R u) dt \quad (15)$$

while simultaneously subjected to the system model constraints in (12) and the control input in (13). This problem formulation resembles the one of a Linear-Quadratic Regulator (LQR), which requires a linear system model and a state feedback control in order to compute the optimal control gains. Therefore, we need to linearize the system in (12) around an adequate linearization point. Intuitively this should be one of the two equilibrium points, $x_1^* = [0 \ 0]^T$ or $x_2^* = [\omega_{ss} \ 0]^T$, before and after the disturbance. However, since $\frac{\partial f}{\partial D}|_{x_1^*, u^*} = 0$ and $\frac{\partial f}{\partial M}|_{x_2^*, u^*} = 0$, a single linearization does not provide a model that could sufficiently capture the adaptive nature of the proposed controller. Furthermore, an LQR based on the system linearized around a non-equilibrium operating point would tend to drive the system back to the same unstable point, which is not desirable. Therefore, we propose two different linearization and control design methods in order to implement a *multi-LQR* scheme and overcome this issue.

B. Method A: Two Independent Controllers

The first method is based on the assumption that the system damping has little effect in the initial stages of a frequency response, whereas the system inertia has low impact in the later stages. These two phases are separated by the time instance of reaching the frequency nadir, thus dividing the response time into $[0, t_m)$ and $[t_m, +\infty)$, with $u_M = M$ and $u_D = D$ being the only control input, respectively.

The initial stage of the system response, i.e., $t \in [0, t_m)$, can be characterized by linearizing the system in (12) around (x_1^*, u_M^*) , while assuming a constant $D = D^*$ throughout the sequence, which yields:

$$\begin{aligned} \underbrace{\begin{bmatrix} \dot{\omega} \\ \dot{\omega} \end{bmatrix}}_{\dot{x}_M} &= \underbrace{\begin{bmatrix} 0 & 1 \\ -\frac{D^*+R_g}{TM^*} & -(\frac{D^*+F_g}{M^*} + \frac{1}{T}) \end{bmatrix}}_A \underbrace{\begin{bmatrix} \omega \\ \dot{\omega} \end{bmatrix}}_{\dot{x}_M} + \underbrace{\begin{bmatrix} 0 \\ \frac{-\Delta P}{TM^{*2}} \end{bmatrix}}_{B_M} \Delta M \\ \underbrace{\begin{bmatrix} \omega_0 \\ \dot{\omega}_0 \end{bmatrix}}_{x_{M0}} &= \begin{bmatrix} 0 \\ \dot{\omega}(0^+) \end{bmatrix}, \quad \Delta M = -\underbrace{\begin{bmatrix} K_m & \hat{K}_m \end{bmatrix}}_{K_M} \begin{bmatrix} \omega \\ \dot{\omega} \end{bmatrix} \end{aligned} \quad (16)$$

Similarly, the period $t \in [t_m, +\infty)$ is described using the linearization around (x_2^*, u_D^*) and a no-feedback inertia control, resulting in:

$$\begin{aligned} \underbrace{\begin{bmatrix} \dot{\omega} \\ \dot{\omega} \end{bmatrix}}_{\dot{x}_D} &= \underbrace{\begin{bmatrix} 0 & 1 \\ -\frac{D^*+R_g}{TM^*} & -(\frac{D^*+F_g}{M^*} + \frac{1}{T}) \end{bmatrix}}_A \underbrace{\begin{bmatrix} \hat{\omega} \\ \dot{\omega} \end{bmatrix}}_{\dot{x}_D} + \underbrace{\begin{bmatrix} 0 \\ \frac{-\omega_{ss}}{TM^*} \end{bmatrix}}_{B_D} \Delta D \\ \underbrace{\begin{bmatrix} \hat{\omega}_0 \\ \dot{\omega}_0 \end{bmatrix}}_{x_{D0}} &= \begin{bmatrix} \omega_m - \omega_{ss} \\ 0 \end{bmatrix}, \quad \Delta D = -\underbrace{\begin{bmatrix} K_d & \hat{K}_d \end{bmatrix}}_{K_D} \begin{bmatrix} \hat{\omega} \\ \dot{\omega} \end{bmatrix} \end{aligned} \quad (17)$$

where $\omega_m = \omega(t_m)$ and $\hat{\omega} = \omega - \omega_{ss}$.

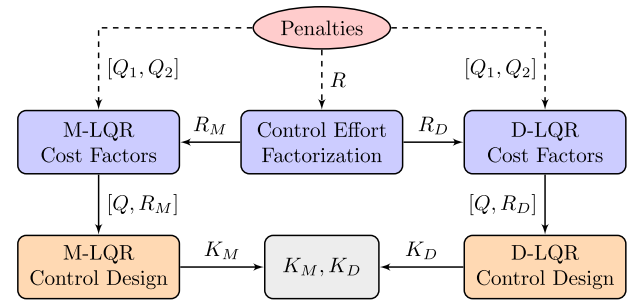


Fig. 3. Multi-LQR control design in *Method A*.

In order to achieve a trade-off between the frequency response and the control effort, the following general form of a two-fold optimization problem is used to derive the controllers:

$$\min_{x_i, u_i} \int_{t_{1,i}}^{t_{2,i}} (x_i^T Q x_i + \Delta u_i^T R_i \Delta u_i) dt \quad (18a)$$

$$\text{s.t.} \quad \dot{x}_i = A x_i + B_i \Delta u_i \quad (18b)$$

$$\Delta u_i = -K_i x_i \quad (18c)$$

with $Q = \text{diag}(Q_1, Q_2)$ and index $i \in \{M, D\}$ denoting the corresponding multi-LQR formulation, from now on termed M-LQR and D-LQR respectively. The two controllers have different state space models, state vectors and control inputs but also the weight R in the objective function corresponding to the control effort penalty differs. This allows to distinguish between the different nature of energy utilization in the two stages. Furthermore, the integral spans over different time intervals, corresponding to the aforementioned two stages of the frequency response. For a given set of cost penalties (Q, R) the optimization in (18) yields the optimal feedback control gains $K_i^* = R_i^{-1} B_i^T P_i$, where P_i is the solution to the following algebraic Riccati equation:

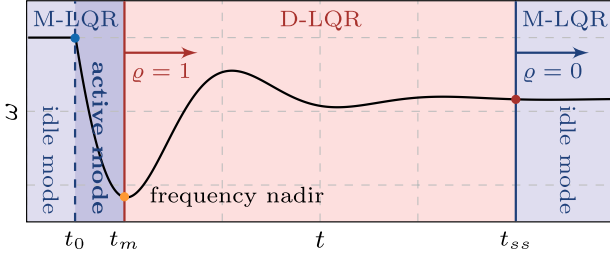
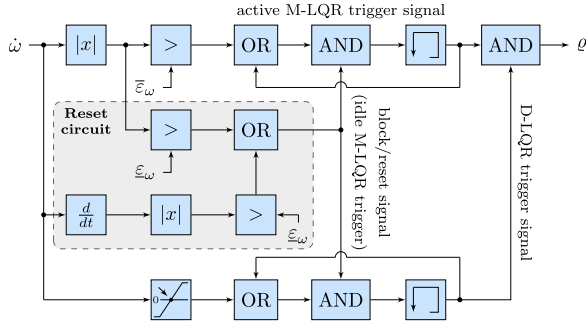
$$A^T P_i + P_i A - P_i B_i R_i^{-1} B_i^T P_i + Q = 0 \quad (19)$$

The two control designs can be completed independently, as shown in Fig. 3, with the control effort factorization providing the cost penalties R_D and R_M under the following ratio:

$$R_M = R, \quad R_D = R \left(\frac{\Delta M_{\max}}{\Delta D_{\max}} \right)^2 \approx R \left(\frac{\omega_{\max}}{\dot{\omega}_{\max}} \right)^2 \quad (20)$$

The approximation is based on equating the energy content of the two controllers during peak power injection, which according to the dynamics of the swing equation corresponds to the ratio of frequency nadir and maximum RoCoF.

The application of a multi-LQR scheme in *Method A* consists of a continuous alternation between the two algorithms, with D-LQR being initialized at the instance of frequency nadir ($\varrho = 1$) and remaining active until the frequency stabilization threshold (ε_ω) has been met. As soon as the system reaches equilibrium the M-LQR control mode is employed ($\varrho = 0$), as depicted in Fig. 4, where the blue and red dots refer to the respective linearization points. The *idle* mode corresponds to a pre-disturbance period, where the control gains are kept the same as for the previous M-LQR sequence. Once the fault is detected through a RoCoF threshold ($\bar{\varepsilon}_\omega$) the new K_M gains are computed and the *active*

Fig. 4. Application of a multi-LQR scheme in *Method A*.Fig. 5. Signal logic scheme for LQR detection in *Method A*.

M-LQR mode is initiated. In order to generate an adequate trigger signal (ϱ), the signal logic scheme incorporates three main circuits as presented in Fig. 5: (i) a fault detection block that employs a RoCoF threshold ($\bar{\varepsilon}_\omega$) to ignite the active M-LQR mode; (ii) a D-LQR trigger signal using zero-crossing of RoCoF; and (iii) a block/reset signal based on frequency stabilization (idle M-LQR trigger).

C. Method B: Two Dependent Controllers

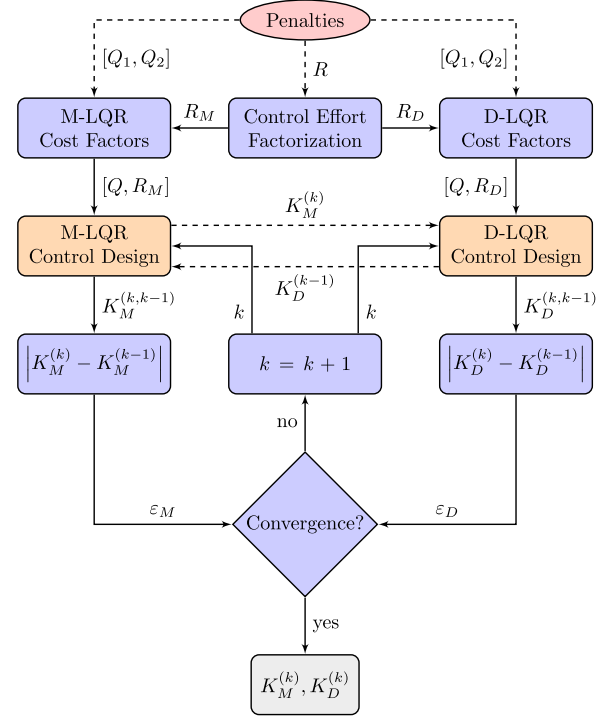
The second approach attempts to fully capture the properties of both control inputs by designing a cooperative control of the two LQR-based controllers. This is achieved through an iterative exchange of optimal control gains between the two consecutive LQR computations visualized in Fig. 6. The linearization practice is kept the same as for *Method A*.

Let us start with the M-LQR design. The same notation as in Section II-B is used. Unlike the previous method where we assumed $D = D^*$, here we include the adaptive damping control from (17) of the form:

$$D = D(\omega, \dot{\omega}) = D^* - \underbrace{[K_d \quad \hat{K}_d]}_{K_D} \begin{bmatrix} \omega - \omega_{ss} \\ \dot{\omega} \end{bmatrix} \quad (21)$$

with K_D being the known parameter obtained in the previous update of D-LQR. The system in (12) can now be transformed as follows:

$$\begin{bmatrix} \dot{\omega} \\ \ddot{\omega} \end{bmatrix} = \begin{bmatrix} 0 & 1 \\ -(\frac{D(\omega, \dot{\omega}) + R_g}{TM}) & -(\frac{D(\omega, \dot{\omega}) + F_g}{M} + \frac{1}{T}) \end{bmatrix} \begin{bmatrix} \omega \\ \dot{\omega} \end{bmatrix} + \begin{bmatrix} 0 \\ \frac{\Delta P}{TM} \end{bmatrix} = f(\omega, \dot{\omega}, M, D(\omega, \dot{\omega})) \quad (22)$$

Fig. 6. Multi-LQR control design in *Method B*.

which after the linearization around (x_1^*, u_M^*) yields:

$$\begin{bmatrix} \dot{\omega} \\ \ddot{\omega} \end{bmatrix} = \underbrace{\begin{bmatrix} 0 & 1 \\ -\frac{D^* + R_g + K_d \omega_{ss}}{TM^*} & -(\frac{D^* + F_g}{M^*} + \frac{1}{T}) \end{bmatrix}}_{A_M} \begin{bmatrix} \omega \\ \dot{\omega} \end{bmatrix} + \underbrace{\begin{bmatrix} 0 \\ -\frac{\Delta P}{TM^{*2}} \end{bmatrix}}_{B_M} \Delta M = A_M(K_d) \begin{bmatrix} \omega \\ \dot{\omega} \end{bmatrix} + B_M \Delta M \quad (23)$$

Similarly, we can assume K_M as a known parameter and define the adaptive inertia control for D-LQR as

$$M = M(\omega, \dot{\omega}) = M^* - \underbrace{[K_m \quad \hat{K}_m]}_{K_M} \begin{bmatrix} \omega \\ \dot{\omega} \end{bmatrix} \quad (24)$$

which gives us a closed-loop, non-linear system of the form:

$$\begin{bmatrix} \dot{\omega} \\ \ddot{\omega} \end{bmatrix} = \begin{bmatrix} 0 & 1 \\ -\frac{D + R_g}{TM(\omega, \dot{\omega})} & -(\frac{D + F_g}{M(\omega, \dot{\omega})} + \frac{1}{T}) \end{bmatrix} \begin{bmatrix} \omega \\ \dot{\omega} \end{bmatrix} + \begin{bmatrix} 0 \\ \frac{\Delta P}{TM(\omega, \dot{\omega})} \end{bmatrix} = f(\omega, \dot{\omega}, M(\omega, \dot{\omega}), D) \quad (25)$$

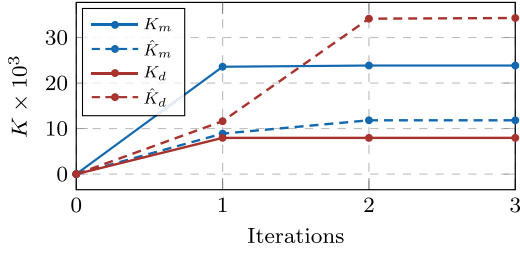


Fig. 7. Iteration progress of control gains in Algorithm 1.

Finally, the expression for the linearized model around (x_2^*, u_D^*) can be computed as:

$$\begin{aligned} \begin{bmatrix} \dot{\hat{\omega}} \\ \ddot{\hat{\omega}} \end{bmatrix} &= \underbrace{\begin{bmatrix} 0 & 1 \\ -\frac{D^*+R_g}{\kappa T} & -(\frac{D^*+F_g}{\kappa} + \frac{1}{T}) \end{bmatrix}}_{A_D} \begin{bmatrix} \hat{\omega} \\ \dot{\hat{\omega}} \end{bmatrix} + \underbrace{\begin{bmatrix} 0 \\ -\frac{\omega_{ss}}{\kappa T} \end{bmatrix}}_{B_D} \Delta D \\ &= A_D(K_m) \begin{bmatrix} \hat{\omega} \\ \dot{\hat{\omega}} \end{bmatrix} + B_D(K_m) \Delta D \end{aligned} \quad (26)$$

where $\kappa = M^* - K_m \omega_{ss}$.

Algorithm 1: Iterative Computation of Optimal Control Gains.

- 1: Set $k = 0$ and $\varepsilon = 0$
 - 2: Initialize system in open-loop $\triangleright K_M^{(0)} = K_D^{(0)} = 0$
 - 3: **while** $\varepsilon > \epsilon$ or $k = 0$ **do**
 - 4: $k = k + 1$
 - 5: Run M -LQR $= f(K_D^{(k-1)})$ \triangleright derive $K_M^{(k)}$
 - 6: Run D -LQR $= f(K_M^{(k)})$ \triangleright derive $K_D^{(k)}$
 - 7: Compute error terms $\triangleright \varepsilon_M = \left| K_M^{(k)} - K_M^{(k-1)} \right|$
 $\triangleright \varepsilon_D = \left| K_D^{(k)} - K_D^{(k-1)} \right|$
 - 8: Determine convergence error $\triangleright \varepsilon = \varepsilon_M + \varepsilon_D$
 - 9: **end while**
 - 10: Return $K_M^{(k)}, K_D^{(k)}$
-

Understandably, the multi-LQR optimization problem in *Method B* resembles the one in (18), with the two main exceptions: (i) both LQRs are infinite, i.e., $[t_{1,i}, t_{2,i}] = [0, +\infty)$; and (ii) the state-space model in (18b) is replaced with $\dot{x}_i = A_i x_i + B_i \Delta u_i$. However, due to the numerical interdependence between the matrices $A_M(K_d)$, $A_D(K_m)$ and $B_D(K_m)$, the two LQR systems can not be solved independently as in *Method A*. Instead, they are iterated until convergence between the consecutive steps is achieved, as proposed in Algorithm 1. As a result, a single, uniform control is obtained, which simplifies the implementation compared to the previous method.

The performance of Algorithm 1 is presented in Fig. 7 which shows the iterative progress of the optimal control gain computation. Due to the complexity of a closed-form solution of the combined Riccati equations, the possibility for deriving an analytic convergence criterion is restricted. However, the fast convergence can be justified by analyzing the mathematical

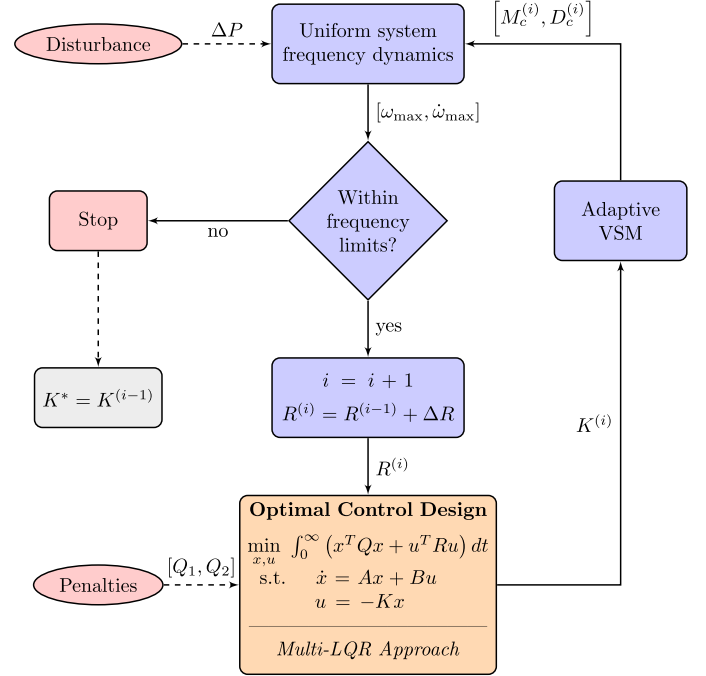


Fig. 8. System-level control design algorithm.

properties of the control design in *Method B*. Since the algorithm is initialized at $K_M^{(0)} = K_D^{(0)} = 0$, the computation of the first M-LQR is done inefficiently without inclusion of adaptive damping. With adaptive inertia control in place, the damping feedback can be reasonably determined for $k = 1$. The inaccuracy of $\hat{K}_m^{(1)}$ and $\hat{K}_d^{(1)}$ is a sole consequence of the linearization, i.e., the fact that the LQR design stabilizes the inverter around the equilibrium where the influence of $\dot{\omega}$ is negligible. This problem is resolved in the second iteration, as both $\hat{K}_m^{(2)}$ and $\hat{K}_d^{(2)}$ are appropriately readjusted, with feedback gains corresponding to ω remaining constant. Therefore, the convergence condition is guaranteed within 3 iterations. This sequence also explains the gradual reduction of convergence error: the first iteration computes all four control gains initially set to zero, whereas the second one only tunes the two gains corresponding to the state feedback $\dot{\omega}$.

D. Parametrization and Implementation

The expression in (19) implies that the selection of cost factors Q and R comprehensively determines the optimal control gains, thus highlighting the importance of cost parametrization. One of the most common (initial) LQR tuning approaches is to consider all objective costs equally [18], i.e., to select the respective weights such that

$$Q_1(\omega_{\max})^2 = Q_2(\dot{\omega}_{\max})^2 = R_i(\Delta u_{i,\max})^2 \quad (27)$$

This is usually achieved by fixing one penalty factor, in our case $Q_1 = (\omega_{\max})^{-2}$ and $Q_2 = (\dot{\omega}_{\max})^{-2}$, and adjusting the cost of control accordingly. Since the optimal selection of $(\Delta M_{\max}, \Delta D_{\max})$ is unclear, we propose an iterative procedure within the optimal control design scheme, as shown in Fig. 8.

Starting from $R^{(0)} \approx 0$, the algorithm yields a maximum penalty and thus a minimum control effort, that still ensures maintaining the frequency and RoCoF within the given bounds. As a result, a uniform 1-D look-up table of the form $K^* = T_{PK}(\Delta P)$ is generated, which provides the optimal feedback gain scheduling for any given system-level disturbance ΔP .

E. Stability Assessment

In this section, we focus on deriving the sufficient stability conditions for adaptive VSM design. Based on the Lyapunov stability theorem, and assuming a justifiable approximation of the form $R_M K_M \approx R_D K_D$, the asymptotic stability of the system is guaranteed under the following tuning condition:

$$\frac{M^*}{T} + D^* + F_g < \frac{M^* - \sqrt{M^{*2} - 4\hat{K}_m \Delta P}}{4\hat{K}_m / K_m} \quad (28)$$

Proof: We start the proof by finding an appropriate candidate Lyapunov function of a nonlinear open-loop system. Similar to the stability analysis of a synchronous generator in [19], we calculate the respective energy function by neglecting the $\dot{\omega}$ term associated to damping in the second equation of (12), and multiply the whole expression with $M\dot{\omega}$ in order to express energy:

$$M\dot{\omega}\ddot{\omega} + \frac{1}{T}((D + R_g)\omega - \Delta P)\dot{\omega} = 0 \quad (29)$$

Integrating the product from the first equilibrium point x_1^* to any point on the system transient trajectory yields the following Lyapunov function:

$$\begin{aligned} V &= E_k + E_p \\ &= \int_0^{\dot{\omega}} M\dot{\omega}d\dot{\omega} + \frac{1}{T} \int_{\omega_{ss}}^{\omega} ((D + R_g)\omega - \Delta P)d\omega \\ &= \frac{1}{2}M\dot{\omega}^2 - \frac{1}{T} \left[\Delta P(\omega - \omega_{ss}) - \frac{1}{2}(D + R_g)(\omega^2 - \omega_{ss}^2) \right] \end{aligned} \quad (30)$$

where $V(\omega, \dot{\omega})$ represents the transient energy of the system in $(\omega, \dot{\omega})$ coordinates after a step disturbance ΔP .

Let us now consider the adaptive approach with $M(\omega, \dot{\omega})$ and $D(\omega, \dot{\omega})$ being functions of state variables through VSM feedback control described in (13). By analyzing the gradient ∇V of the proposed Lyapunov function we can determine its stationary points:

$$\begin{bmatrix} \frac{\partial V}{\partial \omega} \\ \frac{\partial V}{\partial \dot{\omega}} \end{bmatrix} = \begin{bmatrix} \frac{1}{2} \frac{\partial M}{\partial \omega} \dot{\omega}^2 - \frac{1}{T} \left(\Delta P - \frac{1}{2} \frac{\partial D}{\partial \omega} \Delta \omega^2 - \omega(D + R_g) \right) \\ \frac{1}{2} \frac{\partial M}{\partial \dot{\omega}} \dot{\omega}^2 + M\dot{\omega} + \frac{1}{2T} \frac{\partial D}{\partial \dot{\omega}} \Delta \omega^2 \end{bmatrix}$$

where $\Delta \omega^2 \equiv \omega^2 - \omega_{ss}^2$. It can easily be shown that the proposed Lyapunov function has a stationary point at the system equilibrium x_2^* , i.e., $\nabla V(x_2^*) = 0$, which satisfies the first condition of Lyapunov stability. The second condition states that it must be positive definite in the vicinity of the equilibrium point. This can be verified using the Hessian matrix \mathcal{H}

$$\begin{bmatrix} \frac{\partial^2 V}{\partial \omega^2} & \frac{\partial^2 V}{\partial \omega \partial \dot{\omega}} \\ \frac{\partial^2 V}{\partial \dot{\omega} \partial \omega} & \frac{\partial^2 V}{\partial \dot{\omega}^2} \end{bmatrix} = \begin{bmatrix} \frac{1}{T}(D + R_g - 2K_d\dot{\omega}) & -K_m\dot{\omega} \\ -K_m\dot{\omega} & M - 2\hat{K}_m\dot{\omega} \end{bmatrix}$$

which yields the following expression at the aforementioned equilibrium x_2^* :

$$\mathcal{H}(x_2^*) = \begin{bmatrix} \frac{1}{T}(D + R_g - \frac{2\kappa}{D^* + R_g}) & 0 \\ 0 & M \end{bmatrix} \quad (31)$$

Here, $\kappa > 0$ denotes the product $K_d \Delta P$, always positive by the nature of our control design. Having in mind that M , D and R_g are also positive, according to Sylvester's theorem $\mathcal{H}(x_2^*) \succ 0$ holds, and thus V is a valid Lyapunov candidate function.

In order to guarantee asymptotic stability, $\dot{V} = \partial V / \partial t$ has to be positive $\forall t \in [0, \infty)$:

$$\begin{aligned} \dot{V} &= \frac{\partial V}{\partial \dot{\omega}} \frac{\partial \dot{\omega}}{\partial t} + \frac{\partial V}{\partial \omega} \frac{\partial \omega}{\partial t} + \frac{\partial V}{\partial M} \frac{\partial M}{\partial t} + \frac{\partial V}{\partial D} \frac{\partial D}{\partial t} \\ &= - \left(\frac{M}{T} + D + F_g \right) \dot{\omega}^2 + \underbrace{\frac{1}{2} \frac{\partial M}{\partial t} \dot{\omega}^2}_{\nu_M} + \underbrace{\frac{1}{2T} \frac{\partial D}{\partial t} (\omega^2 - \omega_{ss}^2)}_{\nu_D} \end{aligned} \quad (32)$$

Let us now compare the last two terms of (32) by considering their ratio

$$\frac{\nu_M}{\nu_D} = \frac{T \frac{\partial M}{\partial t} \dot{\omega}^2}{\frac{\partial D}{\partial t} (\omega^2 - \omega_{ss}^2)} = \frac{T \dot{\omega}^2}{\omega^2 - \omega_{ss}^2} K_M \circ K_D^{-1} \quad (33)$$

Based on the LQR design and respective cost factor selection, we can assume the following approximation²:

$$K_M \circ K_D^{-1} \approx \frac{R_D}{R_M} = \left(\frac{\omega_{\max}}{\dot{\omega}_{\max}} \right)^2 \quad (34)$$

and hence the ratio in (33) can be transformed into

$$\frac{\nu_M}{\nu_D} \approx \frac{T R_D \dot{\omega}^2}{R_M (\omega^2 - \omega_{ss}^2)} = T \underbrace{\frac{\omega_{\max}^2 \dot{\omega}^2}{\dot{\omega}_{\max}^2 (\omega^2 - \omega_{ss}^2)}}_{\sigma} \quad (35)$$

We can observe that $\sigma > 1$ for high values of ν_M and ν_D during the initial transients, whereas $\nu_M \approx \nu_D = 0$ in steady state. Therefore, it is valid to assume $\nu_M + \nu_D \approx \nu_M$ and neglect the last term in (32), leading to the following condition for system stability:

$$\frac{M}{T} + D + F_g > \frac{1}{2} \frac{\partial M}{\partial t} = \frac{1}{2} (-K_m \dot{\omega} - \hat{K}_m \ddot{\omega}) \quad (36)$$

with the left hand side lower bounded by

$$\frac{M}{T} + D + F_g > \frac{M^*}{T} + D^* + F_g \quad (37)$$

As for the right hand side of (36), we know that both $\dot{\omega}$ and $\ddot{\omega}$ are decaying oscillations, as well as that during the initial stages of the response, when $\frac{\partial M}{\partial t}$ is relatively large, $-K_m \dot{\omega} > 0$ and $-\hat{K}_m \ddot{\omega} < 0$. Hence, we could neglect the term $-\hat{K}_m \ddot{\omega}$ and upper bound the right hand side:

$$-\frac{1}{2} K_m \dot{\omega}_{\max} = -\frac{1}{2} K_m \dot{\omega}(0) > \frac{1}{2} (-K_m \dot{\omega} - \hat{K}_m \ddot{\omega}) \quad (38)$$

²Symbol \circ denotes the element-wise Schur product.

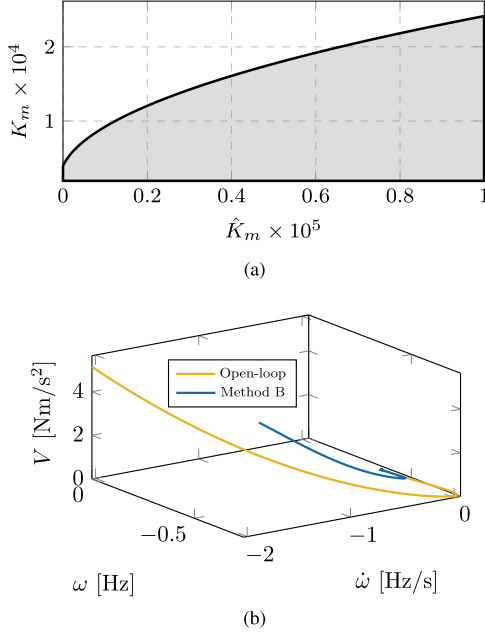


Fig. 9. Stability analysis of the adaptive VSM control design. (a) Stability region of inertia feedback gains. (b) Transient energy trajectory after a step disturbance.

From (36)-(38), a sufficient condition for asymptotic stability is derived as follows:

$$\frac{M^*}{T} + D^* + F_g > -\frac{1}{2} K_m \dot{\omega}_{\max} \quad (39)$$

where

$$\dot{\omega}_{\max} = \frac{M^* - \sqrt{M^{*2} - 4\hat{K}_m \Delta P}}{2\hat{K}_m} \quad (40)$$

Combining (39) and (40) yields the stability condition in (28), which concludes the proof. ■

The aforementioned condition also has a physical interpretation. Since M^*/T term corresponds to damping, this stability margin indicates that the system damping has to be higher than the maximum rate of change of inertia. In other words, the proportional inertia feedback gains (K_m, \hat{K}_m) are bounded by the shaded stability region depicted in Fig. 9(a). Furthermore, as a proof of concept, the proposed Lyapunov function is analyzed based on the respective simulation results. The results shown in Fig. 9(b) indicate that $V(\omega, \dot{\omega})$ remains positive, with transient energy trajectory preserving a decaying trend throughout the disturbance period and converging to zero, thus verifying the system stability. Furthermore, we can observe that the final equilibrium point is x_2^* , as previously discussed.

It should be noted that the suggested stability assessment applies only to *Method B*, since M and D gains vary discontinuously in *Method A* due to explicit switching. However, this can be resolved by approximating the derivative terms $\partial M/\partial t$ and $\partial D/\partial t$ by their average values at the point of switching instance and conducting a similar analysis. As we consider *Method B* to be a more sophisticated and efficient approach of the two, the other stability proof is omitted for brevity.

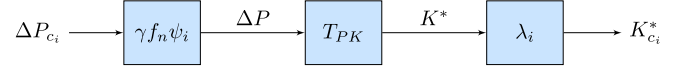


Fig. 10. Individual control scheme for optimal gain selection.

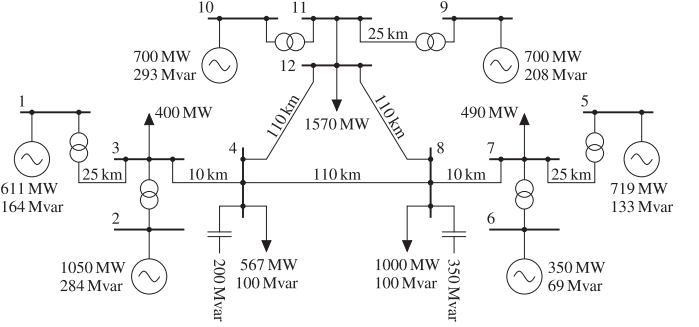


Fig. 11. Topology of the investigated 3-area test system: the converter-based generation is placed at nodes 2, 6, and 10.

F. Multi-Inverter Extension

In order to implement the aforementioned adaptive control design on a large-scale, multi-inverter system, the information of the global power imbalance (ΔP) should be extracted from a locally measured disturbance (ΔP_{c_i}) at the terminal of each VSM unit $i \in \mathcal{N}_v$. Such signal can be obtained as follows:

$$\begin{aligned} \Delta P &= \gamma f_n R_{c_i} \frac{\Delta P_{c_i}}{P_{c_i}} = \gamma f_n \underbrace{(D_{c_i} P_{c_i})^{-1}}_{\psi_i} \Delta P_{c_i} \\ \gamma &= D_l P_{l_0} + \frac{1}{f_n} \sum_{i \in \mathcal{N}_e} \frac{P_{c_i}}{R_{c_i}} \end{aligned} \quad (41)$$

with f_n denoting the nominal frequency and γ mimicking the traditional composite frequency response characteristic (β) of synchronous generators in a low-inertia system; P_{l_0} and D_l are the load power at nominal frequency and its sensitivity to frequency changes, whereas $R_{c_i} = D_{c_i}^{-1}$ is the respective droop equivalent of a VSM-based controller [16]. The traditional generators are omitted from the computation of γ due to high time constants and a significantly slower frequency regulation compared to VSCs. Once ΔP is determined, the optimal feedback gain of the combined VSM control can be obtained from the look-up table, as shown in Fig. 10. A sharing property of the control effort is achieved via proportional scaling factors of the form $\lambda_i = P_{c_i} / \sum_i P_{c_i}$, assuming proportional participation.

IV. MODELING AND CONTROL DESIGN

The proposed adaptive VSM controller is implemented within a state-of-the-art VSC control scheme previously described in [20], where the outer control loop consists of active and reactive power controllers providing the output voltage angle and magnitude reference by adjusting the predefined setpoints (x^*)

according to a measured power imbalance:

$$\begin{aligned}\dot{\omega}_{c_i} &= \frac{1}{M_{c_i}}(p_{c_i}^* - p_{c_i}) - \frac{1}{M_{c_i}}D_{c_i}(\omega_{c_i} - \omega_{c_i}^*), \quad \forall i \in \mathcal{N}_v \\ \omega_{c_j} &= \omega_{c_j}^* + R_{c_j}^p \left(p_{c_j}^* - \frac{\omega_z}{\omega_z + s} p_{c_j} \right), \quad \forall j \in \mathcal{N}_d \\ v_{c_k} &= v_{c_k}^* + R_{c_k}^q \left(q_{c_k}^* - \frac{\omega_z}{\omega_z + s} q_{c_k} \right), \quad \forall k \in \mathcal{N}_c\end{aligned}\quad (42)$$

with $R_{c_j}^p$ and $R_{c_k}^q$ denoting the active and reactive power droop gains, ω_z representing the LPF cut-off frequency, M_{c_i} and D_{c_i} being the adaptive control gains, and $\hat{\theta}_{c_k} = \omega_{c_k} \omega_n$. The first two expressions indicate the difference between the VSM and droop-based inverters. Subsequently, the reference voltage vector signal ($v_{c_k} \angle \theta_{c_k}$) is passed through a virtual impedance block, as well as the inner control loop consisting of cascaded voltage and current controllers. The output is combined with the DC-side voltage in order to generate the modulation signal m . In order to detect the system frequency at the connection terminal, a PLL-based synchronization unit is included in the model. However, for the purposes of a grid-forming converter this unit is bypassed via $\omega^* = \omega_n$. The complete mathematical model consists of 13 states and is implemented in per unit. More details on the overall converter control structure and employed parametrization can be found in [15], [16], [20].

For synchronous generators, we consider a traditional model equipped with a prime mover and a *TGOVI* governor. Furthermore, the automatic voltage regulator based on a simplified excitation system *SEXS* is incorporated, together with a *PSSIA* power system stabilizer [21]. Internal machine dynamics are characterized by the transients in the rotor circuits described through flux linkage, as transients in the stator windings decay rapidly and can thus be neglected. The inclusion of stator circuit balance completes the set of differential-algebraic equations, which combined with 6 controller states and swing equation dynamics yields a standard 12th order system. For more details regarding the generator modeling and internal parameter computation, we refer the reader to [22].

V. RESULTS

As proof of concept, we test the proposed method on a modified version of a well investigated Kundur's 2-area system shown in Fig. 11, consisting of 3 areas and 6 generators. The same test case has been previously used in several studies on placement and effects of inertia and damping in low-inertia systems [23], [24]. Furthermore, we consider a scenario where three traditional generators are replaced with converter-based units. In order to validate the uniform frequency formulation from Section II, a loss of synchronous generator at node 5 is simulated using a detailed EMT model developed in MATLAB Simulink and compared against the analytic formulation in (6). Understandably, such contingency leads to unacceptable frequency excursion under the open-loop VSM control, indicated by the frequency nadir of ≈ 0.7 Hz in Fig. 12. Nonetheless, the resulting response verifies the accuracy of the proposed uniform approach.

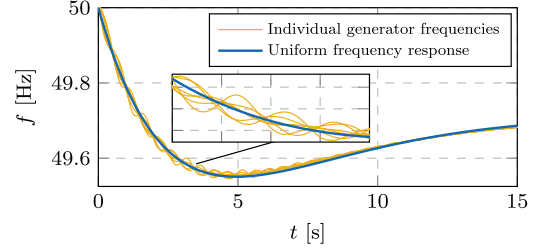


Fig. 12. Frequency response after a 250 MW load increase.

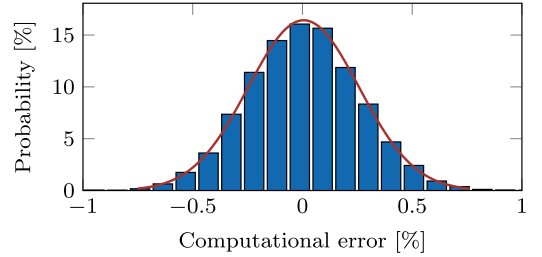


Fig. 13. Error distribution of frequency nadir computation.

Having in mind that the adaptive control gains are computed offline, a risk of inadequate system information pertains to overall error propagation, especially regarding the frequency metric expressions in (6)-(10). This potential issue is investigated using a rigorous parametric sensitivity analysis, with all relevant unit parameters arbitrarily selected within a $[10 - 500]\%$ range of the nominal values. We study a system consisted of $N_g = 1000$ synchronous and inverter-based generators, and consider $N_s = 10^5$ different configuration scenarios. In each scenario, a set of 100 units is randomly removed in order to account for the generators that could potentially be offline. Subsequently, the frequency nadir is analytically computed and compared to its respective value in the full system. The distribution of the computational error shown in Fig. 13 verifies the robustness of the modeling approach, as the worst case mismatch is kept below 1%, and 95% of the scenario set is within a 0.5% error range. For the purposes of our control design, a small margin corresponding to the maximum computational error is added to ω_{\max} and $\dot{\omega}_{\max}$ terms, such that the frequency response of the system always meets the predefined ENTSO-E criteria.

In contrast to open-loop, the adaptive VSM schemes fulfill their purpose of alleviating the disturbance and improve the frequency response in terms of nadir and maximum RoCoF, as illustrated in Fig. 14. The impact of the cost penalty selection is reflected in the frequency nadir reaching the prescribed ENTSO-E under-frequency load shedding threshold of 0.5 Hz. *Method A* achieves a marginally faster convergence rate due to an explicit switch from M-LQR to D-LQR control mode at the instance of reaching the frequency nadir, which is also the reason for the discontinuity in the RoCoF curve due to a sudden step change in M . On the contrary, the additional damping during the initial stages of the response in *Method B* aids the control of the frequency nadir, thus activating less inertia compared to the previous method. This however leads to a slightly higher

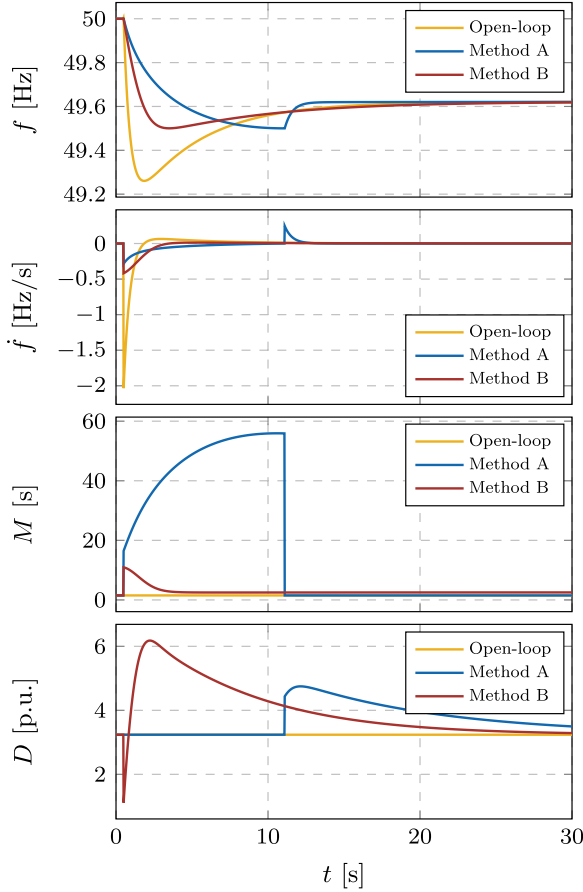


Fig. 14. System response under different VSM control designs: (i) frequency; (ii) RoCoF; (iii) inertia; (iv) damping.

maximum RoCoF, which is a well-justified trade-off considering that the RoCoF is significantly below the predefined limit of 1 Hz/s. Nonetheless, the characteristics are reversed in the second stage, as more inertia and less damping is provided by *Method B* than by *Method A*. Another interesting observation is the initial undershoot of damping in *Method B*; a consequence of the D-LQR trying to effectively reach its linearization point x_2^* . This “non-minimum phase” characteristic occurs however only for very large disturbances, with the steady-state frequency well below the 50 Hz mark.

The activation of M and D reveals the distinctive nature of the two algorithms. *Method A* is restricted solely to adaptive inertia as a mean of frequency regulation during the initial response (M-LQR), which directly acts on RoCoF through the explicit $M\dot{\omega}$ term. The effectiveness of such an approach is however limited, since the impact of inertia decays over time, together with $\dot{\omega}$. As a result, the inertia gain is overdimensioned, leading to high depletion of energy and a noticeable spike at the switching instance between two LQRs. In contrast, the combined effort of inertia and damping in *Method B* achieves a qualitatively similar system performance with a more natural frequency response and less energy consumption, as indicated in Fig. 15. We therefore conclude that *Method B* is both a more efficient and practical approach for adaptive VSM design.

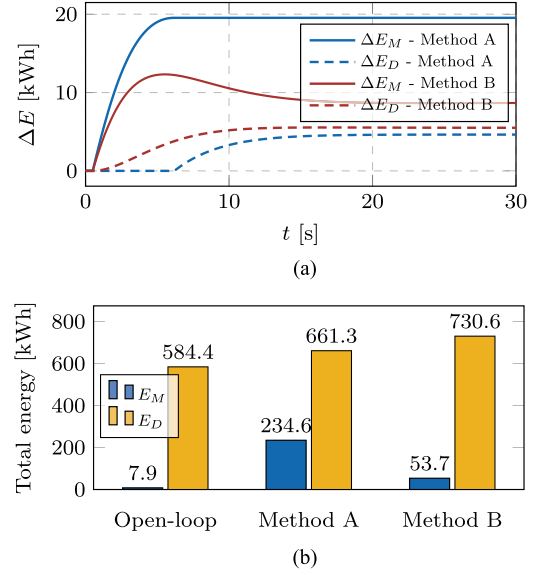


Fig. 15. Energy utilization for containing a loss of generator. (a) Components of the additional control effort. (b) Total energy content.

Some insightful conclusions regarding the two control concepts can be drawn from the energy content of the control effort, with respective energy terms computed as $\Delta E_M = \int \Delta M \dot{\omega} dt$ and $\Delta E_D = \int \Delta D \omega dt$. First of all, it clarifies the decision in the latter approach to compensate inertia with damping during high RoCoF instances, since the ΔE_M term would have a predominant impact on the total costs. Moreover, it can be observed that *Method B* reduces the total energy use of the adaptive control by $\approx 12.5\%$. The increase in total battery utilization compared to the open-loop VSM can be justified by the small size of the test system that makes it highly vulnerable to a loss of generator which accounts for 20 % of total base power. Nonetheless, this is just a fraction ($\approx 1\%$) of the total energy capacity of a 100 MW/129 MWh lithium-ion Hornsdale Power Reserve battery in South Australia, better known as “Tesla Big Battery”, which was recently installed and successfully used for similar fast regulation purposes [25]. Considering that the installed power of the aforementioned system is an order of magnitude higher than in the observed test case, the application of our LQR control is well justified.

Finally, the proposed controllers are incorporated into the detailed EMT model and analyzed on the same test case. For simplicity, only the results of *Method B* design are presented. The system frequency response depicted in Fig. 16 validates the control accuracy, as the frequency nadir is kept within the predefined bounds unlike for the open-loop approach. It also verifies that the adaptive VSM control and the accompanying signal processing do not interfere with the cascaded inner loops, nor with the complex synchronous generator controllers.

VI. CONCLUSION

The presented paper introduces a novel distributed VSM concept for converters in power systems with high shares of renew-

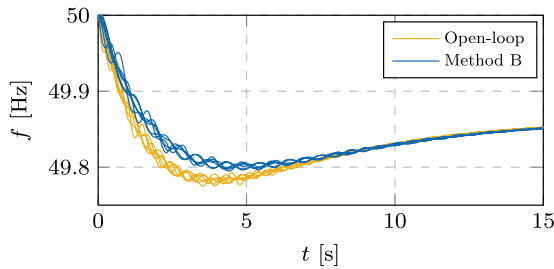


Fig. 16. System frequency response to a loss of synchronous generator in the detailed EMT model: *Method B* vs. open-loop.

able resources. An LQR-based optimal feedback gain is computed to adaptively adjust the emulated inertia and damping constants according to the frequency disturbance in the system, while simultaneously preserving a trade-off between the critical frequency limits and the required control effort. Two control designs have been proposed and compared against the open-loop concept, indicating an overall better frequency response with a reasonable increase in energy consumption. Due to its conceptually superior design, the iterative LQR algorithm in *Method B* is determined to be the more efficient and practical control concept of the two. Furthermore, the adaptive VSM models are included into a detailed converter control scheme and verified through a multi-machine EMT simulation, showing that such control design can be employed in a real-world application.

ACKNOWLEDGMENT

The authors would like to thank O. Stanojev from ETH Zurich for the support in developing and testing the EMT platform.

REFERENCES

- [1] A. Ulbig, T. S. Borsche, and G. Andersson, "Impact of low rotational inertia on power system stability and operation," *IFAC Proc. Vol.*, vol. 47, no. 3, pp. 7290–7297, 2014.
- [2] G. Delille, B. Francois, and G. Malarange, "Dynamic frequency control support by energy storage to reduce the impact of wind and solar generation on isolated power system's inertia," *IEEE Trans. Sustain. Energy*, vol. 3, no. 4, pp. 931–939, Oct. 2012.
- [3] J. Rocabert, A. Luna, F. Blaabjerg, and P. Rodriguez, "Control of power converters in ac microgrids," *IEEE Trans. Power Electron.*, vol. 27, no. 11, pp. 4734–4749, Nov. 2012.
- [4] Q. C. Zhong and G. Weiss, "Synchronverters: Inverters that mimic synchronous generators," *IEEE Trans. Ind. Electron.*, vol. 58, no. 4, pp. 1259–1267, Apr. 2011.
- [5] U. Tamrakar, D. Shrestha, M. Manisha, B. P. Bhattarai, T. M. Hansen, and R. Tonkoski, *Virtual Inertia: Current Trends and Future Directions*. Basel, Switzerland: MDPI AG, Jun. 2017.
- [6] M. Ashabani and Y. A. R. I. Mohamed, "Novel comprehensive control framework for incorporating VSCs to smart power grids using bidirectional synchronous-VSC," *IEEE Trans. Power Syst.*, vol. 29, no. 2, pp. 943–957, Mar. 2014.
- [7] J. Fang, X. Li, and Y. Tang, "Grid-connected power converters with distributed virtual power system inertia," in *Proc. IEEE Energy Convers. Congr. Expo.*, Oct. 2017, pp. 4267–4273.
- [8] J. Morren, S. W. H. de Haan, W. L. Kling, and J. A. Ferreira, "Wind turbines emulating inertia and supporting primary frequency control," *IEEE Trans. Sustain. Energy*, vol. 21, no. 1, pp. 433–434, Feb. 2006.
- [9] N. Soni, S. Doolla, and M. C. Chandorkar, "Improvement of transient response in microgrids using virtual inertia," *IEEE Trans. Power Del.*, vol. 28, no. 3, pp. 1830–1838, Jul. 2013.

- [10] M. A. Torres L., L. A. C. Lopes, L. A. Moran T., and J. R. Espinoza C., "Self-tuning virtual synchronous machine: A control strategy for energy storage systems to support dynamic frequency control," *IEEE Trans. Energy Convers.*, vol. 29, no. 4, pp. 833–840, Dec. 2014.
- [11] J. Alipoor, Y. Miura, and T. Ise, "Power system stabilization using virtual synchronous generator with alternating moment of inertia," *IEEE J. Emerg. Sel. Topics Power Electron.*, vol. 3, no. 2, pp. 451–458, Jun. 2015.
- [12] D. Li, Q. Zhu, S. Lin, and X. Y. Bian, "A self-adaptive inertia and damping combination control of vsg to support frequency stability," *IEEE Trans. Energy Convers.*, vol. 32, no. 1, pp. 397–398, Mar. 2017.
- [13] U. Markovic, Z. Chu, P. Aristidou, and G. Hug, "Fast frequency control scheme through adaptive virtual inertia emulation," in *Proc. IEEE Innovative Smart Grid Technologies*, May 2018.
- [14] P. M. Anderson and M. Mirheydar, "A low-order system frequency response model," *IEEE Trans. Power Syst.*, vol. 5, no. 3, pp. 720–729, Aug. 1990.
- [15] U. Markovic, O. Stanojev, P. Aristidou, and G. Hug, "Partial grid forming concept for 100% inverter-based transmission systems," in *Proc. IEEE PES Gen. Meeting*, Aug. 2018.
- [16] R. Ofir, U. Markovic, P. Aristidou, and G. Hug, "Droop vs. virtual inertia: Comparison from the perspective of converter operation mode," in *Proc. IEEE Int. Energy Conf.*, Jun. 2018.
- [17] H. Ahmadi and H. Ghasemi, "Security-constrained unit commitment with linearized system frequency limit constraints," *IEEE Trans. Power Syst.*, vol. 29, no. 4, pp. 1536–1545, Jul. 2014.
- [18] S. Chandrapati, *Design and Implementation: Linear Quadratic Regulator*. LAP LAMBERT Academic Publishing, 2011. [Online]. Available: <https://www.lap-publishing.com/>
- [19] J. Machowski, J. W. Bialek, and J. R. Bumby, *Power System Dynamics: Stability and Control*. Hoboken, NJ, USA: Wiley, 2008.
- [20] U. Markovic, J. Vorwerk, P. Aristidou, and G. Hug, "Stability analysis of converter control modes in low-inertia power systems," in *Proc. IEEE Innovative Smart Grid Technologies*, Oct. 2018.
- [21] "Documentation on controller tests in test grid configurations," ENTSO-E, Brussels, Belgium, Tech. Rep., Nov. 2013.
- [22] P. Kundur, *Power System Stability and Control*. New York, NY, USA: McGraw-Hill, 1994.
- [23] T. S. Borsche, T. Liu, and D. J. Hill, "Effects of rotational inertia on power system damping and frequency transients," in *Proc. 54th IEEE Conf. Decis. Control*, Dec. 2015.
- [24] D. Groß, S. Bolognani, B. Poolla, and F. Dörfler, "Increasing the resilience of low-inertia power systems by virtual inertia and damping," in *Proc. IREP Bulk Power Syst. Dyn. Control Symp.*, Aug. 2017.
- [25] "Initial operation of the Hornsdale Power Reserve battery energy storage system," AEMO, Melbourne, VIC, Australia, Tech. Rep., Apr. 2018.



Uros Markovic (S'16) was born in Belgrade, Serbia. He received the M.Sc. degree in electrical engineering and information technology from the Swiss Federal Institute of Technology, Zurich, Switzerland, in 2016, where he has been working toward the Ph.D. degree in the power systems laboratory since March 2016. His research interests include power system dynamics and control and optimization, with a focus on stability and operation of inverter-based power systems with low rotational inertia.



Zhongda Chu (S'18) received the M.Sc. degree in electrical engineering and information technology from the Swiss Federal Institute of Technology, Zurich, Switzerland, in 2018. He is currently working toward the Ph.D. degree with the Department of Electrical and Electronic Engineering, Imperial College London, London, U.K. His research interests include control and optimization of low inertia power systems.



Petros Aristidou (S'10–M'15) received the Diploma degree in electrical and computer engineering from the National Technical University of Athens, Athens, Greece, in 2010, and the Ph.D. in engineering sciences from the University of Liège, Liège, Belgium, in 2015. He is currently a Lecturer (Assistant Professor) in smart energy systems with the University of Leeds, Leeds, U.K. His research interests include power system dynamics, control, and simulation.



Gabriela Hug (S'05–M'08–SM'14) was born in Baden, Switzerland. She received the M.Sc. degree in electrical engineering and the Ph.D. degree both from the Swiss Federal Institute of Technology (ETH), Zurich, Switzerland, in 2004 and 2008, respectively. After the Ph.D. degree, she worked with the Special Studies Group of Hydro One, Toronto, ON, Canada, and from 2009 to 2015, she was an Assistant Professor with Carnegie Mellon University, Pittsburgh, PA, USA. She is currently an Associate Professor with the Power Systems Laboratory, ETH Zurich. Her research is dedicated to control and optimization of electric power systems.